Wang ZX, Wang YQ, Yun X, Gardner L and Hu XG. Experimental and numerical study of fixed-ended high strength aluminum alloy angle section columns. ASCE Journal of Structural Engineering, 2020.

Experimental and numerical study of fixed-ended high strength aluminum alloy angle section columns

Zhongxing Wang, Aff.M.ASCE[1]; Yuanqing Wang[2]; Xiang Yun[3]; Leroy Gardner[4]; and Xiaoguang Hu[5]

[1] PhD Student, Department of Civil Engineering, Tsinghua University, Beijing 10084, PR China.

[2] Professor, Department of Civil Engineering, Tsinghua University, Beijing 10084, PR China.

[3] Research Associate, Department of Civil and Environmental Engineering, South Kensington Campus, Imperial College London, London SW7 2AZ, UK.

[4] Professor, Department of Civil and Environmental Engineering, South Kensington Campus, Imperial College London, London SW7 2AZ, UK (corresponding author).

[5] Structural Engineer, China Electric Power Research Institute, Beijing 100055, PR China.

Abstract: High strength aluminum alloys are emerging and gaining increasing prominence in structural engineering. The structural behavior and design of 7A04-T6 high strength aluminum alloy equal-leg angle section columns under axial compression are investigated in this study. Eighteen experiments on extruded high strength aluminum alloy angle section columns with various lengths were carried out. Complementary material tests and initial geometric imperfection measurements were also performed. The test setup, procedure and results, including failure modes, load-carrying capacities and load-end shortening responses, are fully reported. The test program was followed by a numerical study, where refined finite element (FE) models were first developed and validated against the test results and then utilized to carry out parametric analyses covering a wide range of cross-section dimensions and column lengths. Finally, the load-carrying capacities obtained from the tests and numerical analyses were used to evaluate the accuracy of existing design provisions in European, Chinese and American standards for aluminum alloy structures and the direct strength method (DSM). The results showed that the existing design methods generally yield good capacity predictions for

fixed-ended members failing by flexural buckling, but rather conservative and scattered predictions when failure is by flexural-torsional buckling. Improved resistance predictions were achieved through application of a revised DSM-based approach.

Keywords: High strength aluminum alloy; Angle section; Testing; Finite element (FE) analysis; Direct strength method (DSM); Experiments.

Introduction

Use of aluminum alloys in structural engineering dates back about one hundred years. Owing to their advantages of light-weight, good corrosion resistance, ease of fabrication and aesthetic appearance, aluminum alloys have been widely used in space structures, and have also featured in bridges and prefabricated systems (Mazzolani 2004). Recently, wider application of the material has been facilitated by the appearance of a number of structural design codes, including the European standard EN 1999-1-1:2007 (EC9) (CEN 2007), the American aluminum design manual (Aluminum Association 2010), the Chinese code for the design of aluminum structures GB 50429-2007 (MOHURD 2007) and the Australian/New Zealand standard for aluminum structures (AS/NZS 1664.1:1997) (Standards Australia 1997). Types 6063-T5 and 6061-T6 are currently the most commonly used aluminum alloys in construction, with yield strengths of around 200 MPa (Wang et al. 2016a). With ongoing advances in material science and metallurgy, high strength aluminum alloys are now emerging and gradually finding application in structures. High strength aluminum alloys are high-performance materials that combine the advantages associated with ordinary aluminum alloys with high yield strengths up to about 500 MPa. The high strength enables smaller cross-sections to be used, which facilitates rapid construction, making this material well suited to structures located in inaccessible areas (Mazzolani 2006) such as transmission towers built in remote mountainous areas and rapidly assembled structures in military engineering such as the temporary military bridges and

long-span hangars. Inclusion of the high strength aluminum alloy (Type 7A04-T6) investigated in this study is anticipated in the next revision of GB 50429 (MOHURD 2007).

Angle sections are widely used in a range of engineering structures, including electrical transmission towers, trusses, lattice structures and frames (Adluri and Madugula 1996). A number of studies has been carried out to investigate the structural behavior of steel, stainless steel and aluminum alloy angle section columns and to establish corresponding design rules. Young (2004) carried out a series of experiments on fixed-ended cold-formed steel angle section columns with a range of lengths to underpin the development of column buckling curves. Popovic et al. (1999) conducted an equivalent study on pin-ended members. Adluri and Madugula (1996a, b) performed tests on twenty-six hot-rolled steel angle section columns under axial compression failing by flexural buckling and proposed a suitable column buckling curve. Liang et al. (2019) carried out tests on sixteen hot-rolled austenitic stainless steel equal-leg angle section columns; complementary numerical analyses were also performed, with an emphasis on studying flexural-torsional buckling. Zhang et al. (2019) carried out an equivalent investigation into the behavior of cold-formed stainless steel angle section columns. Zhao et al. (2016) conducted experiments on sixteen 6082-T6 aluminum alloy angle section members to study their stability under eccentric compressive loads. Wang et al. (2016b) tested a series of high strength aluminum alloy pin-ended angle section columns failing by flexural buckling, flexural-torsional buckling and local buckling in order to assess the accuracy of existing design rules. New design methods were also established to determine the buckling resistances of angle section columns, based on the continuous strength method (CSM) (Su et al. 2014) and the direct strength method (DSM) (Dinis et al. 2010; Schafer 2008; Silvestre et al. 2013). Although a number of studies has been conducted to investigate the structural behavior of steel, stainless steel and aluminum alloy angle section columns, the behavior of fixed-ended high strength aluminum alloy angle section columns

has yet to be studied. This is therefore the focus of the present paper.

An experimental and numerical investigation into structural behavior of high strength aluminum alloy angle section columns is presented. First, eighteen tests on specimens with various slenderness ratios are reported; complementary material tests and initial geometric imperfection measurements are also described. Numerical validation and parametric studies are then presented. Finally, the experimental and numerical results are used to evaluate the accuracy of design rules in existing standards, including European, Chinese and American codes and a DSM-based design approach.

Experimental investigation

Eighteen experiments were conducted to investigate the structural behavior of high strength aluminum alloy extruded equal-leg angle section columns under axial compression; the studied grade of the alloy was 7A04-T6, which is an Al-Zn-Mg-Cu series high strength and ultra-hard aluminum alloy with a nominal yield strength (or 0.2% proof stress) of about 530 MPa (Wang et al. 2016c). The same nominal cross-section size – equal angle 200×200×24 was used for all tests, as shown in Fig. 1. Six different column lengths were selected to give a range of minor axis slenderness ratios. Each test was repeated three times to assess the consistency of performance. The average values of measured dimensions of all the specimens are presented in Table 1, in which L is the column length, taken as the average value of the lengths at the three edges, b is the section width equal to the average value of six leg widths (i.e. two leg width measurements at each end and two at the mid-height of the specimens) and t is the leg thickness taken as the mean value of thickness-measurements at ten different locations. The nominal fillet radius (r) of the angle section is 18 mm. The columns were labelled such that the key parameters including nominal section width, nominal column length and serial number can be clearly identified; for example, Specimen L200-3900-3 indicates an angle section column with a nominal section width of 200 mm and a nominal column length of 3900 mm, and that this is the third tested specimen among the repeated experiments.

Initial geometric imperfections

The initial geometric imperfections of all the specimens were measured prior to the column tests using the method set out in (Shi et al. 2011), which was also employed in a previous testing program on pin-ended angle section columns (Wang et al. 2016b). The initial geometric imperfections comprised out-of-straightness and twist, both captured through the measurements δ_1, δ_2, δ_3 and δ_4 illustrated in Fig. 2. The maximum values of δ_1 to δ_4 among three cross-sections along the column lengths – the mid-height section and the two quarter-height sections – were measured using a theodolite and vernier caliper, and are reported in Table 1. The reference line for the imperfection values was a straight line connecting the two end points of the member. Positive and negative ("-") values of the imperfection measurements define their direction, as shown in Fig. 2.

Material properties

Tensile coupon tests on the high strength aluminum alloy material were conducted prior to the column tests according to AS1391-2007 (Standards Australia 2007) in a 300 kN hydraulic universal testing machine. The tensile coupons were cut from both legs of the angle section columns along the longitudinal direction and four repeated coupon tests were performed. The dimensions of the tensile coupons are shown in Fig. 3. A pair of strain gauges and an extensometer with a gauge length of 50 mm were used to measure the strain and elongation in the longitudinal direction of the coupons. No visible necking was observed during the material testing process and failure of the tensile coupons was sudden and audible; the fracture surfaces were also generally relatively smooth, as shown in Fig. 4, indicating brittle failure.

The key measured material properties obtained from the tensile coupon tests are presented in Table 2, in which E is the Young's modulus, $f_{0.2}$ is the 0.2% proof (equivalent yield) stress, f_u is the ultimate stress, n is the exponent of the Ramberg-Osgood (R-O) formulation that describes the degree

of roundedness of the stress-strain curve (Ramberg and Osgood 1943) and ε_u is the strain at the ultimate stress. The measured stress-strain curves are shown in Fig. 5, featuring the characteristic rounded stress-strain response of aluminum alloys, which is similar to that of stainless steel (Gardner 2019) and cold-formed steel (Gardner and Yun 2018). The R-O formulation (Ramberg and Osgood 1943) used to describe the stress-strain curves is given by Eq. (1),

$$\varepsilon = \left(\frac{\sigma}{E}\right) + 0.002\left(\frac{\sigma}{f_{0.2}}\right)^n \tag{1}$$

while the fitted curves are shown in Fig. 5, and can be seen to provide an accurate reflection of the measured material response.

Column test configuration and instrumentation

The column tests were conducted in a YES-500 hydraulic compression testing machine, which has a maximum loading capacity of 5000 kN and is shown in Fig. 6. The tests were performed under displacement control at a rate of 0.15 mm/min. Although there were two hemispherical hinges attached to the top and bottom bearing plates, the plates were fixed against rotation during the loading process. An adjustable and reusable device (Wang et al. 2015) was employed to clamp the end sections of the angle section columns, providing fixed end conditions that were fully restrained against twisting about the longitudinal axis and warping. The clamping device comprised thick high strength steel plates and four M20 high strength bolts, as shown in Fig. 7, and eliminated the need for any welding, as required in previous tests (Ban et al. 2013). The adjustable clamping device was able to accommodate any minor differences in size of the end sections of each column.

The columns were aligned with the aid of a laser, before the application of vertical load along the longitudinal axis. Load, lateral displacement at mid-height, end shortening and strain at key positions were recorded throughout the tests. Linearly-varying displacement transducers (LVDTs) 2-1 and 2-2 were used to measure the lateral displacements of the specimens at mid-height and to distinguish between flexural and flexural-torsional buckling modes; LVDTs 2-3 and 2-4 were used to

measure the vertical displacements. Strain gauges 1-1 to 1-6 were used to determine any load eccentricities in the tests and to monitor the strains at the key locations. The layout of the LVDTs and strain gauges is shown in Fig. 8. Load, displacement and strain were collected in real time at 1 sec intervals using an IMP (Isolated Measurement Pod) Data Acquisition System.

Test results

Both flexural buckling (F) and flexural-torsional buckling (FT) were observed in the failure modes of the test specimens. The Specimens L200-3900-1, L200-3900-2 and L200-3900-3 failed by flexural buckling while the remaining specimens exhibited flexural-torsional buckling. The mode of failure was not always straightforward to identify visually from the deformed shapes of the angle section columns; LVDTs 2-1 and 2-2 were therefore utilized to obtain the lateral displacements in order to distinguish between the failure modes: if LVDTs 2-1 and 2-2 measured similar values, the columns had minimal twist and the failure mode was deemed to be predominantly flexural buckling; in contrast, if the readings from LVDTs 2-1 and 2-2 diverged, signifying twisting, the failure mode was deemed to be flexural-torsional buckling. Fig. 9 shows the load versus lateral displacements at mid-height for two of tested columns, as measured by LVDTs 2-1 and 2-2. The response in Fig. 9 (a) is for Specimen L200-3900-3 and signifies a typical flexural buckling mode, while that in Fig. 9 (b) is for Specimen L200-1560-3 and represents a typical flexural-torsional buckling mode.

The deformed specimens are shown in Fig. 10: Fig. 10 (a) shows a typical flexural buckling mode, while Fig. 10 (b) illustrates a typical flexural-torsional buckling mode. All specimens after testing are shown in Fig. 10 (c), though in some cases, there was no evident residual deformation in the specimens after unloading.

The key results from the high strength aluminum alloy angle section column tests are presented in Table 3, where N_{exp} is the experimental ultimate load and Δe is the end shortening at N_{exp}. Repeated

tests generally yielded consistent results with differences in ultimate capacity of less than 5%, though larger discrepancies were observed in the L200-3120 group, with the largest difference, of almost 12%, between Specimens L200-3120-1 and L200-3120-3.

Load versus end shortening curves for all specimens are shown in Fig. 11, where the peak load of each curve is marked with a red circle; the tests were stopped immediately after the load-carrying capacity of the specimens was reached; hence, the descending branch of the curves is relatively short. It can be seen from the figure that the curves within each group almost coincide with each other, confirming the repeatability of the tests, and that the column axial stiffness reduces with increasing slenderness.

Finite element (FE) analysis

Finite element (FE) models of fixed-ended high strength aluminum alloy angle section columns were established using the software package ANSYS (ANSYS 2012). The general characteristics of the models are described in the present section, while validation of the models and parametric studies are set out in the following two sub-sections.

Twenty-noded solid elements, referred to as SOLID186 in the ANSYS element library (ANSYS 2012), were employed to model the angle section columns and the end plates, ensuring that the properties of the fillet radii could be accurately represented. A preliminary mesh sensitivity analysis was first conducted in order to determine a suitable mesh size that provided a sufficient degree of accuracy with acceptable computational time. Fig. 12 shows typical comparisons of numerically obtained load-end shortening curves with different mesh sizes for the longest and shortest columns; the corresponding computational times (CT) are also indicated in the figure. It can be seen from Fig. 12 that a relatively coarse mesh of 10 elements within the width of the leg and 20 elements along the column length is sufficient for the accuracy of the FE models, while refining the mesh further has

negligible effect on the predicted load-carrying capacity. Hence the relatively coarse mesh density was employed throughout all FE models in the present study to save computational effort. The measured material properties obtained from the tensile coupon tests were incorporated into the FE models. Residual stresses in extruded aluminum alloy members have been shown to be quite small (Mazzolani 1995) and hence were not considered in the FE models. The fixed-ended boundary conditions were modeled by restraining all degrees of freedom of the nodes within the top and bottom end plates, except for the longitudinal translation of the nodes at the top end plate, where the axial compressive load was applied. The end plates were tied to the corresponding end sections of the columns using a rigid-body constraint (ANSYS 2012). The measured imperfection amplitudes, as given in Table 1, in conjunction with the critical buckling mode (F or FT) obtained by eigenvalue analysis, was incorporated into the subsequent nonlinear analyses as the initial geometry.

Validation of the FE models

Validation of the developed FE models was conducted by comparing the FE failure modes, load-carrying capacities and load-end shortening responses with those obtained from the experiments. Good agreement between the failure modes of the tested and simulated specimens was obtained, as shown in Fig. 13 for two typical examples. Table 3 presents comparisons of the load-carrying capacities obtained from the FE models (N_{FE}) and the experiments (N_{exp}). As can be seen from Table 3, the load-carrying capacities of the test specimens can be accurately predicted by the FE models, with the mean value of the ratio of N_{FE}/N_{exp} for all specimens being 0.973 and the corresponding coefficient of variation (COV) being 0.064. Good consistency was also observed between the numerical and experimental load-end shortening curves and load-lateral displacement curves; a typical example for each case is illustrated in Figs. 14 and 15, respectively. Moreover, in a parallel study (Wang et al. 2016b), the FE modeling approach employed in this manuscript was further

validated for a wider range of angle cross-sections, but for members with pinned boundary condition. The mean value of N_{FE}/N_{exp} for the 42 specimens is 1.016 with the COV of 0.072, showing good agreement between the FE and experimental results. To sum up, the FE models developed herein can precisely simulate the experimental behavior of fixed-ended high strength aluminum alloy angle section columns under axial compression, confirming their suitability for performing parametric studies to generate data over a wide range of cross-section dimensions and column lengths.

Parametric studies

Upon validation of the FE models, extensive parametric studies were carried out to generate additional structural performance data on fixed-ended high strength aluminum alloy angle section columns under axial compression. The numerically derived results, together with the experimental results, are used in the next section to assess the accuracy of the existing codified design methods (CEN 2007; Aluminum Association 2010; MOHURD 2007) and the revised DSM-based design proposal of Dinis and Camotim (2019).

Parametric studies were performed on 390 columns including 26 equal-leg angle sections with two different leg widths (100 and 200 mm) and various leg thicknesses (from 4 to 32 mm). The width-to-thickness ratios of the legs varied from 4.50 to 21.75, allowing a wide range of cross-section slendernesses to be investigated. Fillet radii were considered in the modeling of the angle sections, with the radius r taken as 12 mm and 18 mm for the angle sections with 100 mm and 200 mm leg widths, respectively. Rounded leg tips with a radius of $t/3$ (see Fig. 1) were also simulated in the FE models. Following the method for determining the values of imperfections in parametric studies reported by Ellobody and Young (2005), the imperfection amplitudes adopted in the parametric studies were taken as the average measured values of the tested specimens ($L/1821$ for out-of-straightness and $0.053t$ for twist). For all the studied columns, positive imperfection values (see Fig.

2) were employed, though the sign of imperfections have minimal influence on the ultimate resistance of fixed-ended angle section columns according to Mesacasa et al. (2014). The failure modes of the high strength aluminum alloy angle section columns can be categorized into three types: local buckling, flexural-torsional buckling and flexural buckling. Since flexural-torsional buckling and flexural buckling are the focus of the present study, the column lengths were selected to avoid local buckling failure. The selected column lengths for each angle section are listed in Tables 4 and 5. According to previous studies (Dinis and Camotim 2015; Zhang et al. 2019), specimens failing by flexural-torsional buckling generally fall within the plateau region of the signature curve i.e. on the graph of the elastic buckling load (P_{cr}) versus the column length (L), as shown in Fig. 16. Note that in the present study, the P_{cr}-L curve for each angle section was obtained using GBTUL (Bebiano et al. 2018), which is numerical analysis software based on Generalized Beam Theory (GBT) (Schardt 1994; Silvestre and Camotim 2002a,b; Camotim et al. 2004). The investigated columns with lengths beyond the plateau region were expected to fail by flexural buckling; these columns are highlighted with an asterisk (*) in Tables 4 and 5.

Comparison of test and numerical results with design standards and other approaches

In this section, the 18 experimental results and 390 numerical results are utilized to access the accuracy of existing design methods provided in the European standard EN 1999-1-1:2007 (EC9) (CEN 2007), the Chinese code for the design of aluminum structures GB 50429-2007 (MOHURD 2007) and the American aluminum design manual (Aluminum Association (AA) 2010), as well as a revised DSM-based design approach (Dinis and Camotim 2019). A quantitative evaluation of the design approaches is reported in Table 6, where N_u is the experimentally (or numerically) obtained load-carrying capacity, and $N_{u,EC9}$, $N_{u,GB}$, $N_{u,AA}$ and $N_{u,DSM}$ are the design load-carrying capacities

determined according to EC9, GB 50429-2007, AA and the DSM, respectively. In all calculations, the measured (or modeled) geometric and material properties have been employed and all partial factors have been set equal to unity. Note that the suffixes 'F' and 'FT' in Table 6 indicate columns failing by flexural buckling and flexural-torsional buckling, respectively.

EN 1999-1-1:2007 (EC9) and GB 50429-2007

EC9 employs different buckling curves for columns failing by flexural buckling and flexural-torsional buckling. According to EC9, the design load-carrying capacity ($N_{u,EC9}$) of an angle section column, without any consideration for welding, is given by Eq. (2),

$$N_{u,EC9}=\frac{\chi A_{eff} f_{0.2}}{\gamma_{M1}} \tag{2}$$

in which γ_{M1} is the partial safety factor for member buckling, A_{eff} is the effective area allowing for local buckling in class 4 cross-sections, but taken as the gross cross-sectional area for angle section columns failing by flexural-torsional buckling, as specified in EC9, and χ is the member buckling reduction factor determined from Eq. (3).

$$\chi=\frac{1}{\phi+\sqrt{\phi^2-\bar{\lambda}^2}}<1.0,\ \text{with}\ \phi=0.5\left(1+\alpha\left(\bar{\lambda}-\bar{\lambda}_0\right)+\bar{\lambda}^2\right) \tag{3}$$

in which α is an imperfection factor, equal to 0.2 for both flexural buckling and flexural-torsional buckling modes, $\bar{\lambda}_0$ is the plateau length of the column buckling curves, equal to 0.1 for flexural buckling and 0.6 for flexural-torsional buckling, and $\bar{\lambda}$ is the non-dimensional slenderness for the relevant buckling mode, which can be calculated from Eq. (4),

$$\bar{\lambda}=\sqrt{\frac{A_{eff} f_{0.2}}{N_{cr}}} \tag{4}$$

in which N_{cr} is the elastic critical load for the relevant buckling mode based on the gross cross-sectional properties. For flexural buckling, N_{cr} is given by:

$$N_{cr} = \frac{\pi^2 EAi^2}{L_{cr}^2} \tag{5}$$

in which L_{cr} is the buckling length in the buckling plane considered, taken as $L/2$ for the fixed-ended columns studied herein and i is the radius of gyration about the relevant axis. The formulae for calculating N_{cr} for flexural-torsional buckling are presented in Annex I.4 of EC9. Note that, in comparison to flexural buckling, N_{cr} for flexural-torsional buckling is more sensitive to the cross-sectional properties than the member length, as highlighted by Zhang et al (2019) in their study on stainless steel angle section columns.

The accuracy of the EC9 provisions for the design of aluminum alloy fixed-ended angle section columns was evaluated through comparisons against the test and FE load-carrying capacities. The test and FE load-carrying capacities, normalized by the product of A_{eff} and $f_{0.2}$, are plotted against the non-dimensional slenderness $\overline{\lambda}$ in Fig. 17, alongside the EC9 design flexural and flexural-torsional buckling curves. It can be observed that the buckling curve for flexural buckling is generally satisfactory, but for angle section columns failing by flexural-torsional buckling, the results are very scattered and the buckling curve is generally conservative. The high scatter in the experimental and numerical data for the flexural-torsional buckling mode indicates that it is not possible to predict the load-carrying capacities of angle section columns failing in this mode accurately using a single buckling curve. As shown in Table 6, the mean value of $N_{uF,EC9}/N_{uF}$ is equal to 0.98, with a COV of 0.016, while the mean value of $N_{uFT,EC9}/N_{uFT}$ is 0.64 with a COV of 0.36, revealing a high level of conservatism and inconsistency in the EC9 predictions for aluminum alloy angle section columns failing by flexural-torsional buckling.

The current Chinese standard GB 50429-2007 employs a similar design method for the calculation of the load-carrying capacities ($N_{u,GB}$) of aluminum alloy angle section columns as that

used in EC9, as given by Eq. (6),

$$N_{u,GB}=\varphi\left(\eta_e A\right)\eta_{as} f_{0.2} \tag{6}$$

in which φ is a buckling coefficient (equivalent to the reduction factor χ in EC9) determined from Eq. (7), η_e is a reduction factor accounting for cross-sectional local buckling and η_{as} is the coefficient of section asymmetry, which can be calculated using Eq. (8).

$$\varphi=\left(\frac{1}{2\overline{\lambda}^2}\right)\left\{\left[1+\alpha\left(\overline{\lambda}-\overline{\lambda}_0\right)+\overline{\lambda}^2\right]-\sqrt{\left[1+\alpha\left(\overline{\lambda}-\overline{\lambda}_0\right)+\overline{\lambda}^2\right]-4\overline{\lambda}^2}\right\}\le 1 \tag{7}$$

$$\eta_{as}=1-2.4\left(\frac{y_{max}-y_{min}}{h}\right)^2\left(\frac{\overline{\lambda}^2}{\left(1+\overline{\lambda}^2\right)+\left(1+\overline{\lambda}\right)^2}\right) \tag{8}$$

In Eq. (7), α and $\overline{\lambda}_0$ are taken as 0.2 and 0.15, respectively, for both flexural and flexural-torsional buckling implying that only a single column buckling curve is used for angle section columns in GB 50429-2007. However, for columns with mono-symmetric cross-sections, such as equal-leg angle sections, failing by flexural-torsional buckling, an equivalent slenderness λ_{yw}, taking due consideration of the torsional effect is employed, after normalization, in place of of $\overline{\lambda}$; the formula for λ_{yw} is given in Section 7.2 of GB 50429-2007 and has the same definition as the equivalent slenderness ratio λ_e used in the American aluminum design manual which is detailed in the next sub-section. In Eq. (8), y_{max} and y_{min} are the larger and smaller values of the distances between the extreme outer edges and the centroid of the cross-section, respectively, and h is the sum of y_{max} and y_{min}. In the present study, η_{as} is equal to 1.0 for all the investigated aluminum alloy angle section columns.

Fig. 18 shows comparisons of the experimental and numerical results with the column buckling curve provided in GB 50429-2007, while Fig. 19 depicts comparisons between the EC9 and GB 50429-2007 predictions, where the ratios of $N_{u,code}/N_u$ (i.e. $N_{u,EC9}/N_u$ and $N_{u,GB}/N_u$) are plotted against the non-dimensional slenderness $\overline{\lambda}$. It is evident from Figs 17 and 18 that although the GB 50429-2007 predictions for angle section columns failing by flexural buckling are reasonably good, those

for flexural-torsional buckling are more conservative and scattered than the EC9 predictions. For angle section columns, local and torsional buckling are closely related (Silvestre et al. 2013; Dinis and Camotim 2019), which makes it unnecessary to consider the two buckling effects separately. Since the torsional effect has already been considered in the flexural-torsional buckling curve, no further reduction is made for local bucking in EC9, with A_{eff} taken as A in Eq. (2). However, an additional reduction factor η_{e}, taking account of local buckling, is adopted in GB 50429-2007, leading thus to more conservative predictions than EC9.

American aluminum design manuals (AA)

The design resistance for aluminum alloy angle section columns $N_{\text{u,AA}}$ determined according to the aluminum association (AA 2010) takes the lowest buckling resistance of three modes – member buckling (N_{m}), local buckling (N_{l}) and the interaction between the two (N_{i}), as given by Eq. (9).

$$N_{\text{u,AA}} = \min\left(N_{\text{m}}, N_{\text{l}}, N_{\text{i}}\right) \tag{9}$$

The member buckling resistance N_{m} can be determined from Eq. (10),

$$N_{\text{m}} = \begin{cases} A_g 0.85\left(B_{\text{c}} - D_{\text{c}}\lambda\right) \le A_{\text{g}} f_{0.2} & \text{if } \lambda < S_2 \\ A_{\text{g}} 0.85\pi^2 E / \lambda^2 & \text{if } \lambda \ge S_2 \end{cases} \tag{10}$$

in which A_{g} is the gross area of the cross-section, B_{c} and D_{c} are constants as given in Table B.4.2 of AA, S_2 is the transition slenderness between inelastic buckling and elastic buckling and λ is the column slenderness ratio about the relevant axis. For flexural buckling, $\lambda = L_{\text{cr}}/i$, while for the flexural-torsional buckling mode, λ is taken as the greater of the slenderness ratio for flexural buckling and the equivalent slenderness ratio λ_{e} defined by Eq. (11):

$$\lambda_{\text{e}} = \pi\sqrt{\frac{E}{F_{\text{e}}}} \tag{11}$$

in which F_{e} is the elastic buckling stress, given, for members with singly symmetric cross-sections such as equal-leg angle section columns, by Eq. (12),

$$F_{\mathrm{e}}=\left(\frac{F_{\mathrm{ey}}+F_{\mathrm{ez}}}{2H}\right)\left[1-\sqrt{1-\frac{4F_{\mathrm{ey}}F_{\mathrm{ez}}H}{\left(F_{\mathrm{ey}}+F_{\mathrm{ez}}\right)^{2}}}\right] \tag{12}$$

where F_{ey} is the elastic buckling stresses for buckling about the y-y axis (equivalent to the u-u axis in EC9), F_{ez} is the elastic buckling stress for torsional buckling and H is a geometric parameter associated with the cross-section dimensions, which can be determined from Section E.3.2 of AA.

The local buckling resistance, N_{l} should be calculated using Eq. (13),

$$N_{\mathrm{l}}=\sum_{i=1}^{n}F_{ci}A_i+F_{cy}\left(A_g-\sum_{i=1}^{n}A_i\right) \tag{13}$$

in which F_{ci} and A_i are the local buckling stress and the area of each element i (where there are two equal elements in the case of equal angles), respectively, and F_{cy} is the compressive yield stress.

The local-global interactive buckling resistance, N_{i}, can be calculated from Eq. (14),

$$N_{\mathrm{i}}=\left(\frac{0.85\pi^{2}E}{\lambda^{2}}\right)^{1/3}F_{\mathrm{ei}}{}^{2/3}A_g \tag{14}$$

where F_{ei} is the smallest elastic local buckling stress for all elements, which, in the case of equal angles, is equal to $\pi^2E/(5b/t)^2$.

According to the design provisions of the aluminum association (AA 2010), as planned, none of the tested or modeled high strength aluminum angle section column failed by local buckling and only 22 specimens failed by an interaction between member buckling and local buckling. All the remaining columns, failing by member buckling, are compared to the AA buckling curve in Fig. 20, where $N_{\mathrm{u}}/A_{\mathrm{g}}$ $f_{0.2}$ is plotted on the vertical axis against the slenderness ratio on the horizontal axis. As can be seen from the figure, the AA predictions lie marginally on the unsafe side for specimens failing by flexural buckling but are rather conservative for columns failing by flexural-torsional buckling. As shown in Table 6, the mean values of $N_{\mathrm{uF,AA}}/N_{\mathrm{uF}}$ and $N_{\mathrm{uFT,AA}}/N_{\mathrm{uFT}}$ are equal to 1.02 and 0.67, with the corresponding values of COV equal to 0.053 and 0.310, respectively. Although the AA offers more

accurate strength predictions for high strength aluminum angle section columns failing by flexural-torsional buckling than EC9 and GB 50429-2007, there is clearly scope for improved accuracy and consistency, which is explored in the following sub-section.

Revised DSM-based approach for flexural-torsional buckling

The comparisons set out in the preceding two sub-sections reveal that the considered design rules provide accurate predictions of the load-carrying capacities of fixed-ended high strength aluminum alloy columns failing by flexural buckling. However, the predictions in the case of flexural-torsional buckling are less accurate and more scattered, because the length-dependent and stable post-buckling nature of the flexural-torsional buckling mode of the aluminum alloy angle section columns are not adequately accounted for in the current codes. Similar observations were made for carbon steel angle section columns by Dinis and Camotim (2019), who, as a result, proposed a new design method based on the direct strength method (DSM). The new DSM-based approach was shown to provide more accurate and consistent resistance predictions than existing design methods for fixed-ended carbon steel equal-leg angle section columns failing by flexural-torsional buckling, and is assessed herein for the design of high strength aluminum alloy angle section columns.

The compression resistance of fixed-ended equal-leg angle section columns failing by flexural-torsional buckling $N_{\mathrm{uFT,DSM}}$ (Dinis and Camotim 2019) is given by Eq. (15),

$$N_{\mathrm{uFT,DSM}} = \begin{cases} A_g f_{\mathrm{ne}} & \text{if } \lambda_{\mathrm{fte}} \le \left(0.5+\sqrt{0.25-b}\right)^{-2\mathrm{a}} \\ A_g f_{\mathrm{ne}} \lambda_{\mathrm{fte}}^{-2\mathrm{a}} \left(1-b\lambda_{\mathrm{fte}}^{-2\mathrm{a}}\right) & \text{if } \lambda_{\mathrm{fte}} > \left(0.5+\sqrt{0.25-b}\right)^{-2\mathrm{a}} \end{cases} \tag{15}$$

where λ_{fte} is the interactive slenderness ratio which is equal to the square root of the ratio of the design global buckling stress f_{ne}, determined from Eq. (16), to the elastic critical flexural-torsional buckling stress f_{crft}, which can be calculated from Eq. (17). Note that, the interactive slenderness ratio λ_{fte} considers the interaction between flexural buckling and flexural-torsional buckling.

$$f_{ne}=\begin{cases} f_{0.2}\left(0.658^{f_{0.2}/f_{cre}}\right) & \text{if } \sqrt{f_{0.2}/f_{cre}} \le 1.5 \\ f_{0.2}\left(\dfrac{0.877}{f_{0.2}/f_{cre}}\right) & \text{if } \sqrt{f_{0.2}/f_{cre}} > 1.5 \end{cases} \tag{16}$$

$$f_{crft}=0.8\left(f_{bt}+f_{bf}-\sqrt{\left(f_{bt}+f_{bf}\right)^2-2.5f_{bt}f_{bf}}\right) \tag{17}$$

In Eqs. (16) and (17), f_{cre} is the elastic critical flexural buckling stress about the minor principal axis, f_{bt} is the elastic critical torsional buckling stress, equal to $Gt^2/b^2+\pi^2Et^2/[12(kL)^2]$, where G is the shear modulus, and f_{bf} is the flexural buckling stress about the major axis which is equal to $\pi^2Eb^2/[6(kL)^2]$. In the calculation of f_{cre}, f_{bt} and f_{bf}, the effective length factor k should be taken as 0.5 for the fixed-ended columns. Note that in Eq. (16), $f_{0.2}$ is adopted for the aluminum alloy in place of f_y for carbon steel, but the method is otherwise applied unmodified.

The parameters a and b that appear in Eq. (15), as defined in Eqs. (18) and (19), are a function of the parameter Δ_f, which as given by Eq. (20), is dependent on the ratio of the difference between f_{bt} and f_{crft} to f_{crft}. The lower the value of Δ_f, the greater the influence of the torsional buckling mode, which has more stable post-buckling behavior, and hence the higher the buckling curve. The use of a, b and Δ_f leads to a range of length-dependent buckling curves and results in improved predictions of flexural-torsional buckling resistances.

$$a=\begin{cases} 0.19\Delta_f+0.4 & \text{if } \Delta_f < 3.0 \\ 0.97 & \text{if } \Delta_f \ge 3.0 \end{cases} \tag{18}$$

$$b=\begin{cases} 0.014\Delta_f+0.15 & \text{if } \Delta_f \le 7.0 \\ 0.248 & \text{if } \Delta_f > 7.0 \end{cases} \tag{19}$$

$$\Delta_f=\frac{f_{bt}-f_{crft}}{f_{bt}}\times 100 \tag{20}$$

The applicability of the DSM-based design approach of Dinis and Camotim (2019) to high strength aluminum alloy angle section columns failing by flexural-torsional buckling was evaluated by means of comparisons with the 339 experimental and numerical results generated in the present study. Fig. 21 shows a comparison of the test and FE results with those predicted in accordance with

the DSM-based approach, where good agreement can be observed. A quantitative comparison is presented in Table 6, where the predictions from the DSM-based approach can be seen to be much more accurate and less scattered than the predictions from EC9, GB 50429-2007 and AA, with the mean value of $N_{uFT,DSM}/N_{uFT}$ equal to 0.95 with a corresponding COV of 0.15. The results indicate that the flexural-torsional buckling resistances of high strength aluminum alloy fixed-ended angle section columns can be well predicted using the DSM-based method, though around one third of the predictions lie on the unsafe side. This can be resolved by modifying the buckling curves to reflect the particular characteristics of aluminum alloys, especially non-linear stress-strain responses and strain-hardening behavior. This further scope for improving the DSM-based approach to provide more accurate and reliable predictions for high strength aluminum angle section columns will be explored in future work.

Conclusions

An experimental and numerical investigation into the structural behavior of fixed-ended high strength aluminum alloy equal-leg angle section columns under axial compression has been presented in this paper. The test program comprised tensile coupon tests, initial geometric imperfection measurements and eighteen column tests. FE models were validated against the test results and used to complement the experimental data by a large number of numerical results obtained through an extensive parametric study. Both the test and FE results were used to assess the accuracy of existing design methods for fixed-ended high strength aluminum alloy angle section columns, including the European standard EN 1999-1-1:2007 (CEN 2007), the Chinese code for the design of aluminum structures GB 50429-2007 (MOHURD 2007), the American aluminum design manual (Aluminum Association (AA) 2010), and a new DSM-based design approach (Dinis and Camotim 2019). It was found that the existing design provisions yield accurate predictions for columns failing by flexural buckling, while provide unduly conservative and scattered predictions for columns failing by flexural-

torsional buckling. The new DSM-based design approach was shown to offer more accurate and less scattered predictions for high strength aluminum alloy angle section columns failing by flexural-torsional buckling, though about one third of the predictions lay on the unsafe side, indicating the need for modification of the existing proposals for application to fixed-ended high strength aluminum alloy angle section columns; this is the subject of our ongoing work.

Data availability statement

Some or all data, models, or code that support the findings of this study are available from the corresponding author upon reasonable request.

Acknowledgments

The authors would like to acknowledge the financial support received from the National Natural Science Foundation of China (Grant No. 51038006), the State Grid Corporation of China Science and Technology Project (Grant No. GC71-13-041) and the Special Research Fund for the Doctoral Program of Higher Education (Grant No. 20110002130002). The authors would also like to thank Yuanbin Han and Ying Yu for their contribution to the testing program. The support from the Key Laboratory of Civil Engineering Safety and Durability of China Education Ministry at Tsinghua University is also highly acknowledged.

References

AA (Aluminum Association). (2010). “Aluminum design manual.” Washington, DC.

Adluri, S. M., and Madugula, M. K. (1996a). “Flexural buckling of steel angles: experimental investigation.” *J. Struct. Eng.*, 122(3), 309–317.

Adluri, S. M., and Madugula, M. K. (1996b). “Development of column curve for steel angles.” *J. Struct. Eng.*, 122(3), 318–325.

ANSYS. (2012). *ANSYS software documentation; version 14.5.* Canonsburg, PA; ANSYS.

Ban, H. Y., Shi, G., Shi, Y. J., and Wang, Y. Q. (2013). "Column buckling tests of 420 MPa high strength steel single equal angles." *Int. J. Struct. Stab. Dyn*., 13(2), 60–66.

Bebiano R, Camotim D, and Gonçalves R. (2018). "GBTul 2.0 − A second-generation code for the GBT-based buckling and vibration analysis of thin-walled members." *Thin-Walled Struct.*, 124, 235–257.

Camotim, D., Silvestre, N., Gonçalves, R., and Dinis, P. B. (2004). "GBT analysis of thin-walled members: new formulations and applications." Thin-walled structures: Recent advances and future trends in thin-walled structures technology, J. Loughlan, ed., Canopus, Bath, U.K., 137–168.

CEN (European Committee for Standardization). (2007). "Eurocode 9: Design of aluminum structures—Part 1-1: General rules—General rules and rules for buildings." *BS EN 1999-1-1:2007*, Brussels.

Dinis, P. B., Camotim, D., and Silvestre, N. (2010). "Post-buckling behaviour and strength of angle columns." Proc., Int. Colloquium on Stability and Ductility of Steel Structures (SDSS), E. Batista, P. Vellasco, and L. Lima, eds., Federal Univ. of Rio de Janeiro and State Univ. of Riode Janeiro, Rio de Janeiro, Brazil, 1141–1150.

Dinis, P. B., and Camotim, D. (2015). "A novel DSM-based approach for the rational design of fixed-ended and pin-ended short-to-intermediate thin-walled angle columns." *Thin-Walled Struct.*, 87, 158–182.

Dinis, P. B., and Camotim, D. (2019). "Proposal to Improve the DSM Design of Cold-Formed Steel Angle Columns: Need, Background, Quality Assessment, and Illustration." *J. Struct. Eng.*, 145(8), 04019071.

Ellobody, E., and Young, B. (2005). "Behaviour of cold-formed steel plain angle columns." *J. Struct. Eng.*, 131(3), 457–466.

Gardner, L., and Yun, X. (2018). "Description of stress-strain curves for cold-formed steels." *Constr. Build. Mater.*, 189, 527–538.

Gardner, L. (2019). “Stability and design of stainless steel structures–Review and outlook.” *Thin-Walled Struct.*, 141, 208–216.

Liang, Y., Jeyapragasam, V. V., Zhang, L. L., and Zhao, O. (2019). “Flexural-torsional buckling behaviour of fixed-ended hot-rolled austenitic stainless steel equal-leg angle section columns.” *J. Constr. Steel Res.*, 154, 43–54.

Mazzolani, F. M. (1995). *Aluminium alloy structures*, 2nd Ed., E & FN Spon, London.

Mazzolani, F. M. (2004). “Competing issues for aluminium alloys in structural engineering.” *Prog. Struct. Eng. Mater.*, 6(4), 185–196.

Mazzolani, F. M. (2006). “Structural applications of aluminium in civil engineering.” *Struct. Eng. Int.*, 16(4), 280–285.

Mesacasa, Jr. E., Dinis, P. B., Camotim, D., and Malite, M. (2014). “Mode interaction in thin-walled equal-leg angle columns.” *Thin-Walled Struct.*, 81, 138–149.

MOHURD (Ministry of Housing and Urban-Rural Development of the People’s Republic of China). (2007). “Code for design of aluminium structures.” *GB 50429-2007*, Beijing. (in Chinese)

Popovic, D., Hancock, G. J., and Rasmussen, K. J. (1999). “Axial compression tests of cold-formed angles.” *J. Struct. Eng.*, 125(5), 515–523.

Ramberg, W., and Osgood W. R. (1943). *Description of stress–strain curves by three parameters*. Technical Note No. 902. Washington, DC: National Advisory Committee for Aeronautics.

Schafer, B. W. (2008). “The direct strength method of cold-formed steel member design.” *J. Constr. Steel Res.*, 64(7-8), 766–778.

Schardt, R. (1994). “Generalized beam theory—an adequate method for coupled stability problems.” *Thin-Walled Struct.*, 19(2-4), 161–180.

Shi, G., Ban, H. Y., Shi, Y. J., and Wang, Y. Q. (2011). “Measurement method of the global initial geometric imperfection of structural members.” *China Patent No. 201110117079*, Beijing.

Silvestre, N., and Camotim, D. (2002a). “First-order generalised beam theory for arbitrary orthotropic materials.” *Thin-Walled Struct.*, 40(9), 755–789.

Silvestre, N., and Camotim, D. (2002b). "Second-order generalised beam theory for arbitrary orthotropic materials." *Thin-Walled Struct.*, 40(9), 791–820.

Silvestre, N., Dinis, P. B., and Camotim, D. (2013). "Developments on the design of cold-formed steel angles." *J. Struct. Eng.*, 139(5), 680–694.

Standards Australia. (1997). "Aluminum structures part 1: Limit state design." *AS/NZS 1664.1:1997*, Sydney, Australia.

Standards Australia. (2007). "Methods for tensile testing of metals." *AS 1391-2007*, Sydney, Australia.

Su, M. N., Young, B., and Gardner, L. (2014). "Testing and design of aluminum alloy cross sections in compression." *J. Struct. Eng.*, 140(9), 04014047.

Wang, Y. Q., Wang, Z. X., and Shi, Y. J. (2015). "An adjustable device fixing equal leg angle column precisely in structural experiment." *China Patent No. ZL 2014 2 0609324.0*, Beijing.

Wang, Y. Q., Wang, Z. X., Yin, F. X., Yang, L., Shi, Y. J., and Yin, J. (2016a). "Experimental study and finite element analysis on the local buckling behaviour of aluminium alloy beams under concentrated loads." *Thin-Walled Struct.*, 105, 44–56.

Wang, Y. Q., Wang, Z. X., Hu, X. G., Han, J. K., and Xing, H. J. (2016b). "Experimental study and parametric analysis on the stability behaviour of 7A04 high strength aluminum alloy angle columns under axial compression." *Thin-Walled Struct.*, 108, 305–320.

Wang, Y. Q., Wang, Z. X., Hu, X. G., Han, J. K., Chen, Z. H., and Xing, H. J. (2016c) "Experimental study on the overall stability of 7A04 high strength aluminium alloy angle columns of large section under axial compression." *J. Tianjin Univ. (Sci. Technol.)*, 49(9), 936–943. (in Chinese)

Young, B. (2004). "Tests and design of fixed-ended cold-formed steel plain angle columns." *J. Struct. Eng.*, 130(12), 1931–1940.

Zhang, L. L., Tan, K. H., and Zhao, O. (2019). "Experimental and numerical studies of fixed-ended cold-formed stainless steel equal-leg angle section columns." *Eng. Struct.* 184, 134–144.

Zhao, Y. Z., Zhai, X. M., and Sun, L. J. (2016). "Test and design method for the buckling behaviours of 6082-T6 aluminum alloy columns with box-type and L-type sections under eccentric compression." *Thin-Walled Struct.*, 100, 62–80.

Table 1. Average measured dimensions and initial geometric imperfections of test specimens

Label	Dimensions			Geometric imperfections			
	L (mm)	b (mm)	t (mm)	δ_1 (mm)	δ_2 (mm)	δ_3 (mm)	δ_4 (mm)
L200-1170-1	1171.00	198.88	24.20	0.40	0.84	0.35	0.62
L200-1170-2	1170.70	199.75	24.69	-0.61	0.39	0.54	-0.33
L200-1170-3	1172.45	199.85	24.78	0.50	-0.29	0.54	0.64
L200-1560-1	1562.15	199.48	24.60	0.44	-0.70	-0.29	-0.29
L200-1560-2	1561.10	199.35	24.49	1.20	0.95	0.87	1.04
L200-1560-3	1564.25	198.80	24.30	-0.66	-0.54	1.06	0.67
L200-1950-1	1950.25	199.33	24.74	0.29	-0.65	0.71	0.94
L200-1950-2	1951.95	199.00	24.29	2.23	-1.26	-0.52	0.82
L200-1950-3	1953.15	199.50	24.31	1.56	-0.82	2.97	0.41
L200-2340-1	2343.25	199.23	24.70	0.61	0.76	0.71	-0.74
L200-2340-2	2344.10	199.85	24.78	-1.82	-1.44	0.60	-0.87
L200-2340-3	2341.80	199.15	24.38	0.75	-0.44	0.40	1.43
L200-3120-1	3121.90	199.53	24.58	1.49	2.02	-1.37	1.27
L200-3120-2	3123.50	199.48	24.42	0.48	-1.89	1.46	1.75
L200-3120-3	3121.70	199.33	24.65	0.84	0.82	-0.18	1.39
L200-3900-1	3907.20	198.93	24.24	1.00	0.36	1.75	2.30
L200-3900-2	3905.85	199.73	24.82	2.96	1.95	1.54	2.61
L200-3900-3	3905.00	199.28	24.63	1.07	-2.71	0.42	2.06

Table 2. Measured material properties

Section	Label	E (MPa)	$f_{0.2}$ (MPa)	f_u (MPa)	n	ε_u (%)
L200×200×24	L200-24-1	73000	531.1	582.2	30	7.42
	L200-24-2	71500	530.9	586.0	30	8.00
	L200-24-3	70400	526.3	579.2	30	6.08
	L200-24-4	73100	533.9	601.5	30	7.64
	Average value	72000	530.6	587.2	30	7.29

Table 3. Summary of test and numerical results

Section	Label	L (mm)	N_{exp} (kN)	Δe (mm)	Failure mode	N_{FE} (kN)	N_{FE}/N_{exp}
L200×200×24	L200-1170-1	1171.00	4337.1	8.62	FT	4417.3	1.02
	L200-1170-2	1170.70	4492.1	9.01	FT	4531.4	0.91
	L200-1170-3	1172.45	4326.2	8.61	FT	4575.1	1.06
	L200-1560-1	1562.15	4218.3	11.20	FT	4329.5	1.03
	L200-1560-2	1561.10	4215.4	11.54	FT	4177.8	0.99
	L200-1560-3	1564.25	4079.0	10.90	FT	4141.9	1.02
	L200-1950-1	1950.25	4252.4	12.93	FT	4108.9	0.97
	L200-1950-2	1951.95	3916.7	12.44	FT	3819.8	0.98
	L200-1950-3	1953.15	4012.7	12.58	FT	3812.1	0.95
	L200-2340-1	2343.25	3850.4	14.17	FT	3818.9	0.99
	L200-2340-2	2344.10	3850.4	14.31	FT	3682.3	0.96
	L200-2340-3	2341.80	3769.2	14.61	FT	3717.8	0.99
	L200-3120-1	3121.90	3419.5	17.02	FT	2914.3	0.85
	L200-3120-2	3123.50	3392.5	16.14	FT	2837.6	0.84
	L200-3120-3	3121.70	2997.8	14.96	FT	2915.0	0.97
	L200-3900-1	3907.20	2208.8	14.11	F	2020.5	0.91
	L200-3900-2	3905.85	1958.3	13.28	F	2047.0	1.05
	L200-3900-3	3905.00	2039.6	13.78	F	2084.2	1.02
Mean							0.973
COV							0.064

Table 4. Dimensions of specimens with a section width of 200 mm in parametric analysis

Section	b (mm)	200×200												
	t (mm)	8	10	12	14	16	18	20	22	24	26	28	30	32
Column length (mm)		300	300	350	450	500	500	550	600	650	700	850	950	1000
		400	400	450	550	600	600	600	650	700	800	1000	1200	1200
		500	500	550	650	700	700	700	700	750	900	1200	1400	1400
		600	600	650	750	800	800	800	750	800	1000	1400	1600	1600
		700	700	750	850	900	900	900	800	850	1200	1600	2000	2000
		800	800	850	950	1000	1000	1000	900	900	1400	2000	2400	2400
		900	900	950	1050	1200	1200	1200	1000	1000	1600	2400	2800*	2800*
		1000	1000	1050	1200	1400	1400	1400	1200	1200	2000	2800	3000*	3000*
		1200	1200	1200	1400	1600	1600	1600	1400	1400	2400	3200*	3200*	3200*
		1400	1400	1400	1600	1800	1800	1800	1600	1600	2800	3600*	3400*	3400*
		1600	1600	1600	1800	2000	2000	2000	1800	1800	3200*	4000*	3600*	3600*
		1800	1800	1800	2000	2200	2200	2200	2000	2000	3600*	4400*	3800*	3800*
		2000	2000	2000	2200	2400	2400	2400	2200	2200	4000*	4800*	4000*	4000*
		2200	2200	2200	2400	2600	2600	2600	2400	2400	4400*	5200*	4200*	4200*
		2400	2400	2400	2600	2800	2800	2800	2600	2600	4800*	5600*	4400*	4400*

Note: columns with lengths highlighted with an asterisk (*) expected to fail by flexural buckling.

Table 5. Dimensions of specimens with a section width of 100 mm in parametric analysis

Section	b (mm)	100×100												
	t (mm)	4	5	6	7	8	9	10	11	12	13	14	15	16
Column length (mm)		300	350	400	500	600	600	600	600	600	600	600	600	600
		400	450	500	600	700	650	700	700	700	700	700	700	700
		500	550	600	700	800	700	800	800	800	800	800	800	800
		600	650	700	800	900	750	900	900	900	900	900	900	900
		700	750	800	900	1000	800	1000	1000	1000	1000	1000	1000	1000
		800	850	900	1000	1100	900	1100	1100	1200	1100	1100	1100	1100
		900	950	1000	1100	1200	1000	1200	1200	1400	1200	1200	1200	1200
		1000	1050	1100	1200	1300	1100	1300	1300	1600	1300	1300	1300*	1300*
		1200	1200	1200	1400	1400	1200	1400	1400	1800	1400	1400*	1400*	1400*
		1400	1400	1400	1600	1600	1300	1500	1500	2200*	1600*	1600*	1600*	1600*
		1600	1600	1600	1800	1800	1400	1600	1600	2400*	1800*	1800*	1800*	1800*
		1800	1800	1800	2000	2000	1600	1700	1700	2600*	2000*	2000*	2000*	2000*
		2000	2000	2000	2200	2200	1800	1800	1800	2800*	2200*	2200*	2200*	2200*
		2200	2200	2200	2400	2400	2000	1900	1900	3000*	2400*	2400*	2400*	2400*
		2400	2400	2400	2600	2600	2200	2000	2000*	3200*	2600*	2600*	2600*	2600*

Note: columns with lengths highlighted with an asterisk (*) expected to fail by flexural buckling.

Table 6. Comparison of predicted results with all experimental and numerical results

Comparison	Flexural-torsional buckling (339 data points)				Flexural buckling (69 data points)		
	$N_{uFT,EC9}/N_{uFT}$	$N_{uFT,GB}/N_{uFT}$	$N_{uFT,AA}/N_{uFT}$	$N_{uFT,DSM}/N_{uFT}$	$N_{uF,EC9}/N_{uF}$	$N_{uF,GB}/N_{uF}$	$N_{uF,AA}/N_{uF}$
Mean	0.64	0.57	0.67	0.95	0.98	0.94	1.02
COV	0.36	0.42	0.31	0.15	0.016	0.042	0.053

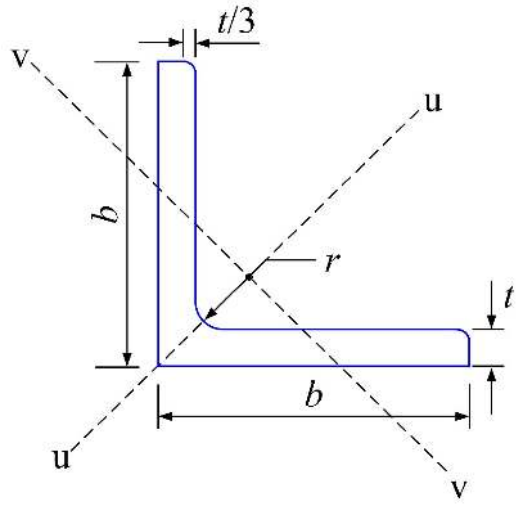

Fig. 1. Schematic diagram of angle section

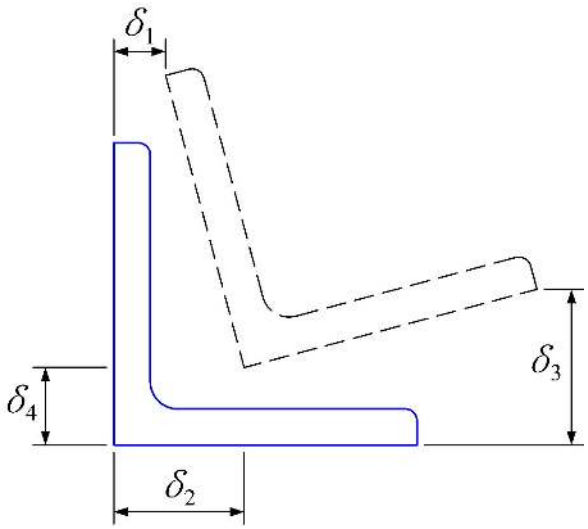

Fig. 2. Schematic diagram of initial geometric imperfection measurements (shown for positive values of δ_i)

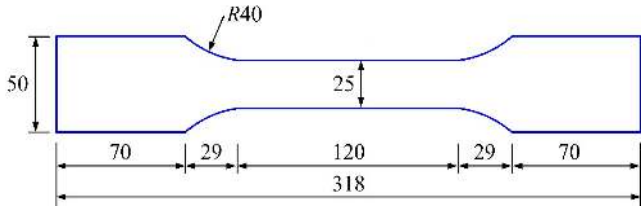

Fig. 3. Dimensions of tensile coupons (dimensions in mm)

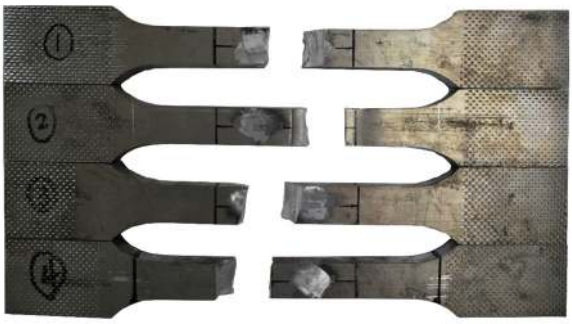

Fig. 4. Tensile coupons after fracture

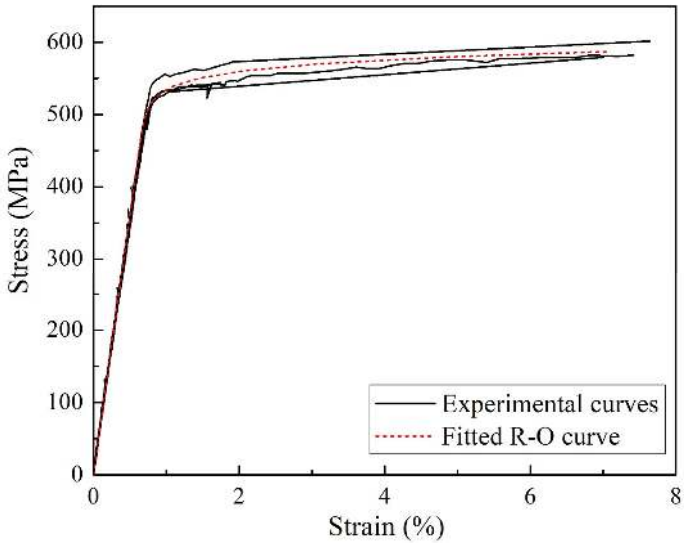

Fig. 5. Experimental stress-strain curves and fitted Ramberg-Osgood (R-O) curve

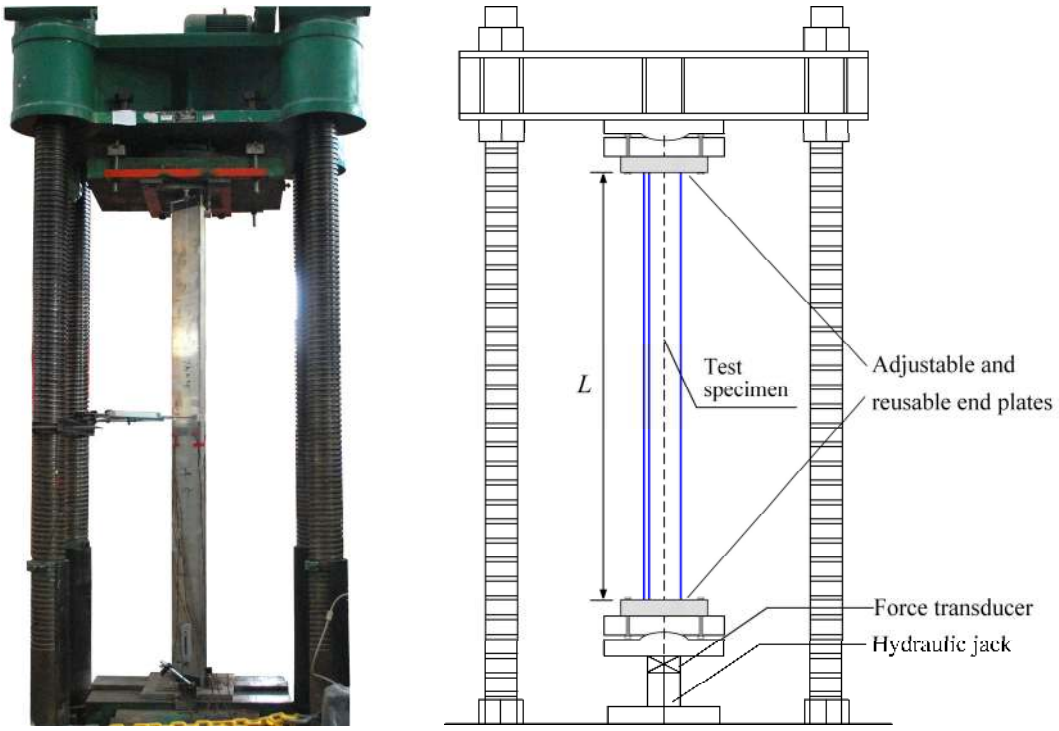

(a) Test set-up (b) Schematic set-up

Fig. 6. Column test set-up

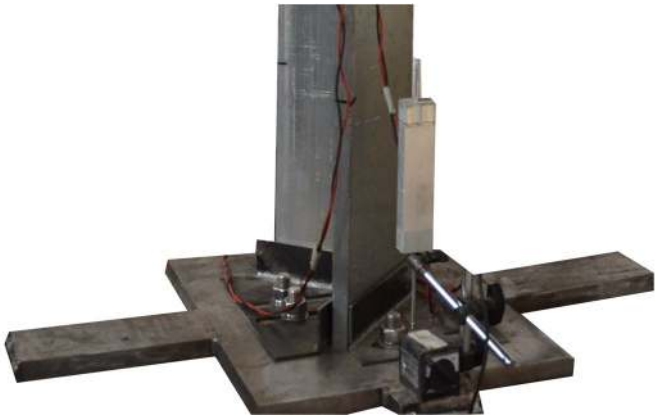

Fig. 7. Adjustable and reusable end plate for angle section column tests

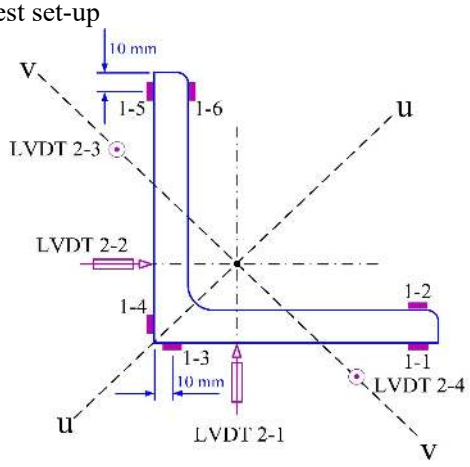

Fig. 8. Layout of LVDTs and strain gauges

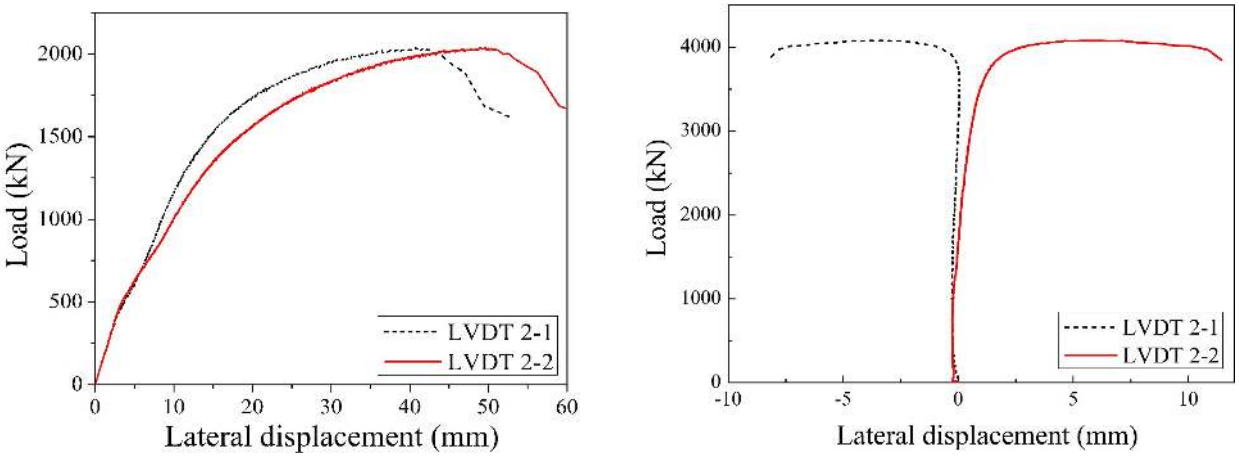

(a) Flexural buckling mode (b) Flexural-torsional buckling mode

Fig. 9. Load versus lateral displacement curves

(a) Flexural buckling mode (b) Flexural-torsional buckling mode (c) All specimens after testing

Fig. 10. Deformed specimens after testing

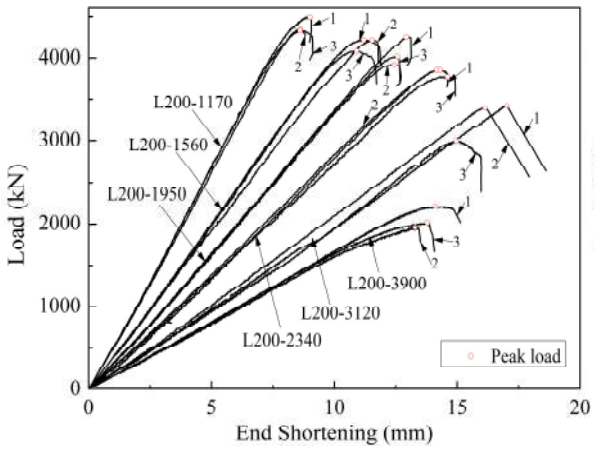

Fig. 11. Load versus end shortening curves from column tests

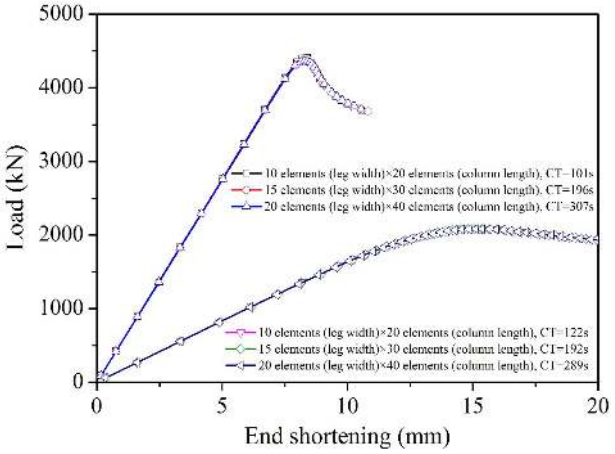

Fig. 12. Results of mesh sensitivity analysis

(a) L200-3120-1 (b) L200-2340-1

Fig. 13. Experimental and numerical failure modes for Specimens L200-3120-1 and L200-2340-1

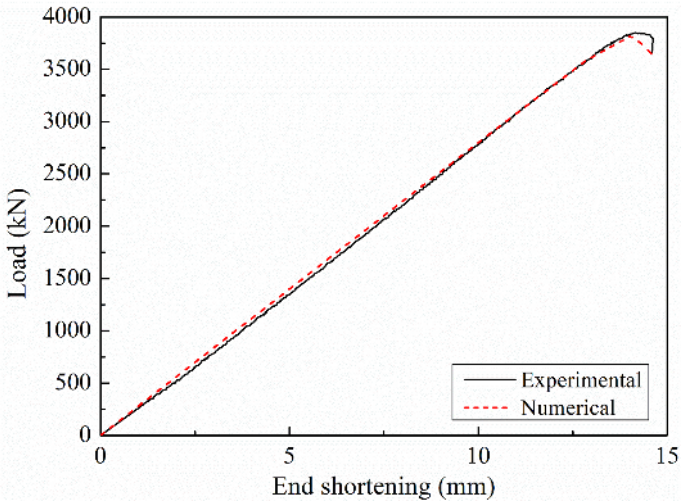

Fig. 14. Experimental and numerical load-end shortening responses for Specimen L200-2340-1

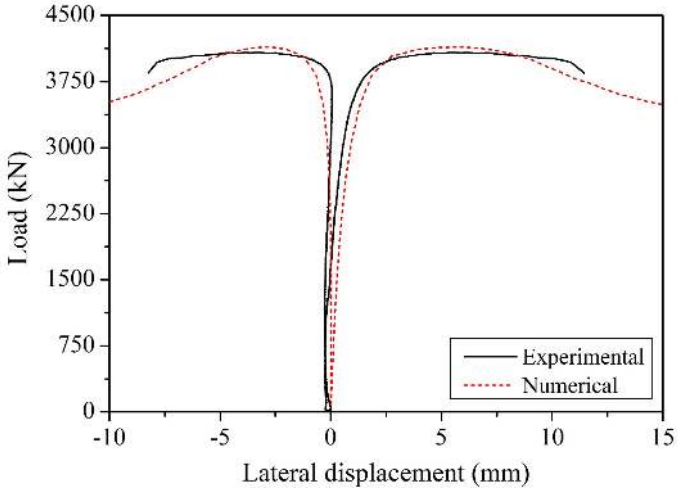

Fig. 15. Experimental and numerical load-lateral displacement responses for Specimen L200-1560-3

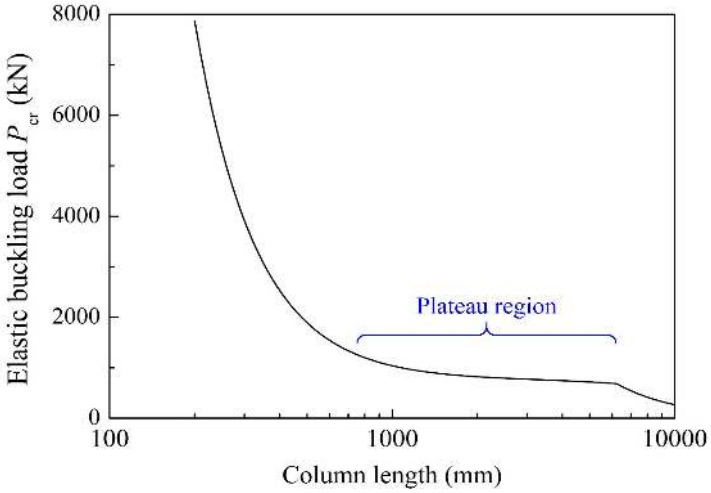

Fig. 16. Elastic buckling load (P_{cr})-column length (L) curve for L200×200×14

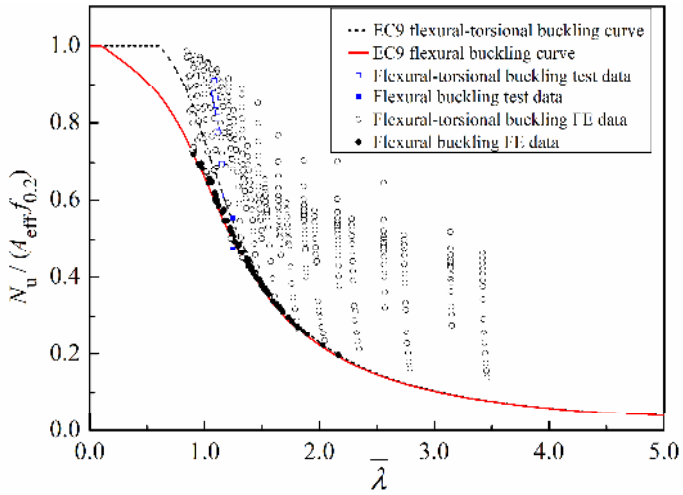

Fig. 17. Comparison of experimental and FE results with EC9 flexural and flexural-torsional buckling curves for high strength aluminum alloy angle section columns

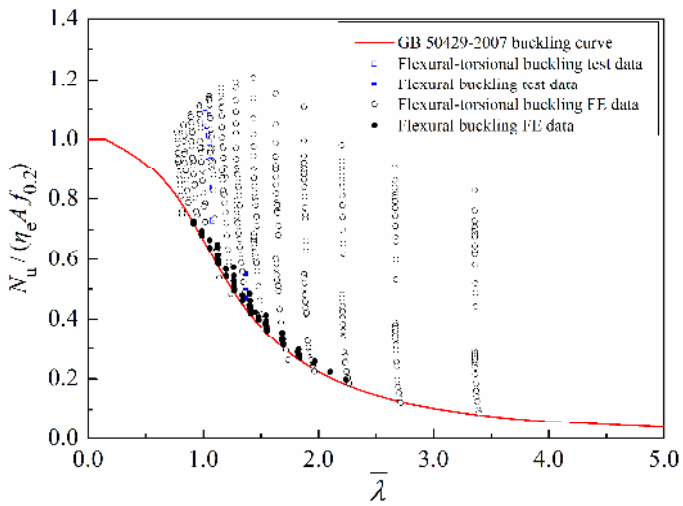

Fig. 18. Comparison of experimental and FE results with GB 50429-2007 flexural and flexural-torsional buckling curve for high strength aluminum alloy angle section columns

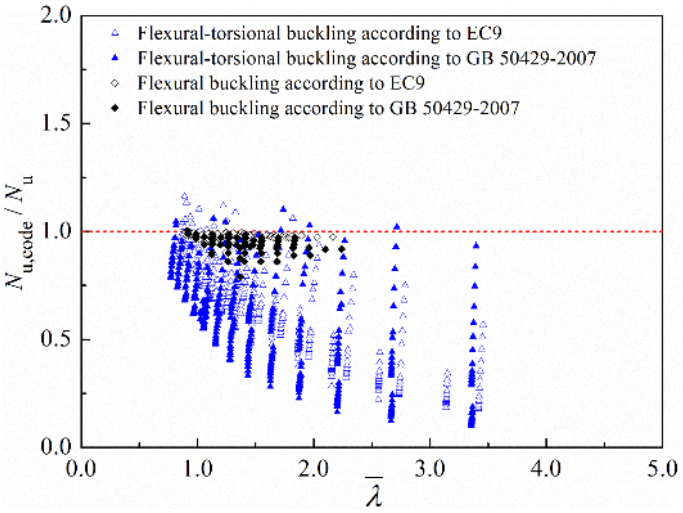

Fig. 19. Assessment of prediction accuracy of EC9 and GB 50429-2007 relative to test and FE results

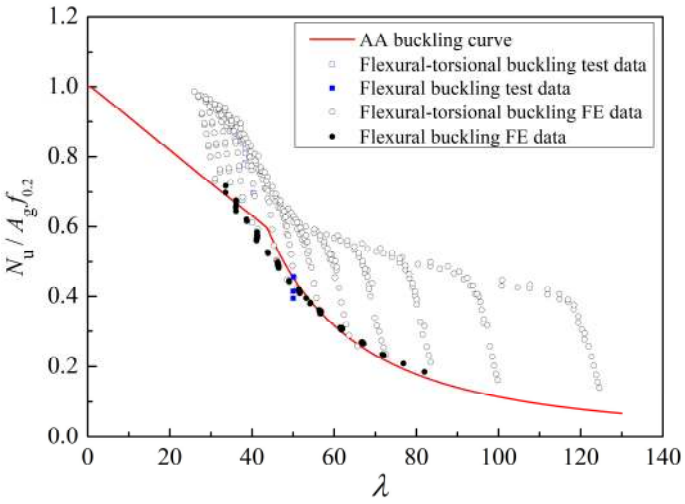

Fig. 20. Comparison of experimental and FE results with AA design curve for high strength aluminum alloy angle columns

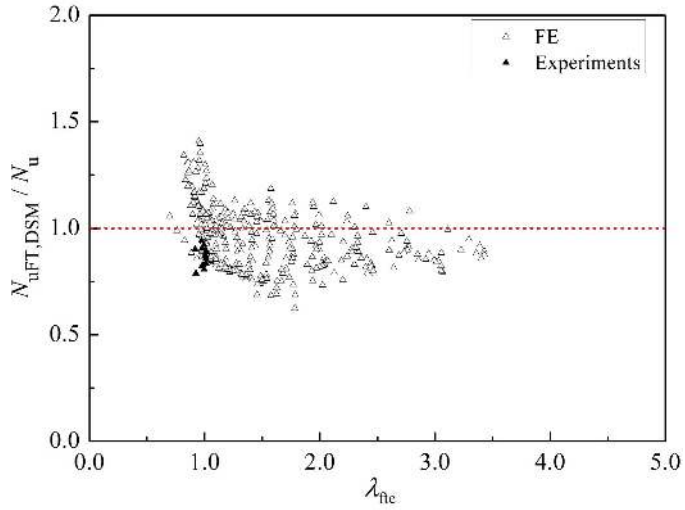

Fig. 21. Comparison of predicted flexural-torsional buckling resistances using the DSM-based approach proposed by Dinis and Camotim (2015) with the experimental and numerical results